Corrosion Behavior and Conductivity of TiNb and TiNbN Coated Steel for Metallic Bipolar Plates

Kun Shi [1], Xue Li [1], Yang Zhao [1], Wei-Wei Li [1], Shu-Bo Wang [1,*], Xiao-Feng Xie [1,2,*], Li Yao [3], Jens Oluf Jensen [4] and Qing-Feng Li [4]

[1] Institute of Nuclear and New Energy Technology, Tsinghua University, Beijing 100084, China;
    shi-k16@mails.tsinghua.edu.cn (K.S.); lixue13@mails.tsinghua.edu.cn (X.L.);
    yzhao16@mails.tsinghua.edu.cn (Y.Z.); willar@mail.tsinghua.edu.cn (W.-W.L.)
[2] Shanxi Research Institute for Clean Energy, Tsinghua University, Taiyuan 030032, China
[3] Advanced Technology Department, SAIC Motor Corporation Limited, Shanghai 201804, China;
    YaoLi01@saicmotor.com
[4] Department of Energy Conversion and Storage, Technical University of Denmark, 2800 Lyngby, Denmark;
    jojen@dtu.dk (J.O.J.); qfli@dtu.dk (Q.-F.L.)
* Correspondence: wangshubo@tsinghua.edu.cn (S.-B.W.); xiexf@tsinghua.edu.cn (X.-F.X.)

check for updates

Abstract: To improve corrosion resistance and electronic conductivity of bipolar plates for proton exchange membrane fuel cells (PEMFC), coatings of TiNb and TiNbN on 316L stainless steel (SS) were prepared by magnetron sputtering. X-ray diffraction measurements confirmed the existence of metallic nitrides in the TiNbN coating. Scanning electron microscope tests showed that the deposited coatings provided smooth surfaces. Further electrochemical measurements indicated that the corrosion resistance of the TiNb coating was significantly higher than that of the substrate. At 0.19 V vs MSE, the long-term stabilized current density of TiNb/316L SS was lower than 1 $\mu A \cdot cm^{-2}$. The interfacial contact resistance values between coating and carbon paper suggested that TiNb and TiNbN films had better contact conductivity than the 316L SS substrate. In conclusion, TiNb coated 316L SS metallic bipolar plate material is a promising option for PEMFC.

Keywords: coating; metallic bipolar plate; PEMFC; TiNb; TiNbN

1. Introduction

The proton exchange membrane fuel cell (PEMFC) is a kind of energy conversion device, which transforms chemical energy into electricity. Owing to its high power-density and zero-emission features, PEMFC has been considered as one of the most prospective power suppliers for vehicles, portable devices and distributed generation [1]. PEMFC is composed of a proton exchange membrane, catalysts, gas diffusion layers, and bipolar plates. The lifetime of PEMFC depends on the durability of individual components. One of the reasons for failure is corrosion of the bipolar plates. This may not only destroy the bipolar plate itself, it also produces ions, which can be detrimental to both membrane [2] and catalyst. Therefore, the corrosion resistance of the bipolar plates is one of the decisive factors influencing the lifetime of a PEMFC. The American Department of Energy (DOE) has established a series of required properties for bipolar plates and one crucial target is to improve corrosion resistance and conductivity [3,4]. Earlier studies concentrated on graphite materials and graphite-based composite bipolar plates [5–7], considering the high corrosion resistance of graphite. However, graphite is brittle and in order to prevent breaking, it is usually machined into quite thick bipolar plate, which increases weight and manufacturing costs of the PEMFC stack [8]. Along with the development of metal forming and welding techniques, metallic bipolar plates have become increasingly relevant for PEMFC due to

the good mechanical strength. This is especially for automotive stacks where weight and volume are critical parameters. In order to reduce cost, the plates should preferably be manufactured as coated inexpensive substrates [9–11]. Austenitic stainless steel (SS), especially 316L, is prone to passivation and can be a suitable bipolar plate material [12,13]. As for coatings, noble metals like Au have been investigated widely [14,15], but although most noble metallic bipolar plates established great corrosion resistance and conductivity, high prices have confined their applications. Compared with noble metals, the low-cost transition metals and transition metal nitrides [16] have showed good performances in PEMFC surroundings attracting significant interest. The niobized 304 SS was reported to a decrease of alloy's corrosion current density, meeting the DOE demand (<1 μA·cm^{-2}) [17]. In acid solution, the corrosion resistance of Ti still needs to be further improved [13]. Metal nitrides such as TiN and NbN have been deposited on different substrates establishing low interfacial contact resistance (ICR). However, after a transient polarization test, the TiN coated sample achieved higher current density than the base SS substrate material [18]. Similarly, the NbN coating's corrosion resistance at high potential also needs to be improved [19]. Considering the embarrassing situation that it is hard to obtain high conductivity and great corrosion resistance at the same time, the idea of mixing Ti, Nb, TiN and NbN properly to combine the best of each of the advantages is proposed. The alloyed TiNb and TiNbN have acceptable prices when applied as films. Additionally, a TiNbN coating can be expected to have attractive mechanical property and has been used in biomedical or mechanical areas [20,21]. TiNb alloys have also been studied earlier for their unique shape memory effect [22]. Aukland et al. [23] evaluated the chemical durability and surface resistances of Ti alloys with 3 at.% Nb and confirmed that the oxidized Ti-3Nb alloys had lower resistances than Ti oxides. However, to the best of our knowledge, there is still a lack of adequate literature investigating the corrosion behavior and conductivity of TiNb or TiNbN coated SS with low Ti content under simulated PEMFC working conditions. As for the deposition method, physical vapor deposition (PVD) provides firm, uniform, and dense coatings compared with electroplating [24]. Among all the PVD ways, magnetron sputtering is used extensively in industry due to its high stability and limited contamination. During sputtering, influenced by electrical and magnetic fields, argon ions in the vacuum chamber bombard the targets causing atoms or clusters to separate from the targets and finally be deposited on the substrate. Usually, coating particles form firm bonds with the base material.

In this study, TiNb and TiNbN coatings with low Ti content were deposited on 316L SS by magnetron sputtering to explore their performances in simulated PEMFC cathode environments. The microstructures, morphologies, and chemical compositions of the coatings were characterized by X-ray diffraction (XRD), scanning electron microscopy (SEM), energy dispersive spectrometry (EDS), and X-ray photoelectron spectroscopy (XPS). Electrochemical experiments and ICR tests were conducted to evaluate the corrosion resistance and conductivity of coated and uncoated 316L SS.

2. Materials and Methods

2.1. Preparation of Coatings

The TiNb and TiNbN coatings were prepared by magnetron co-sputtering and reactive sputtering with a Process Equipment (KJLC, Kurt Company, US) using a radio frequency (RF) Ti target and a direct current (DC) Nb target. The substrate was 316L SS with a thickness of 0.2 mm. Before sputtering, the test specimens were ground with 800, 1500, and 2000 mesh sandpaper, polished with diamond polishing agents and ultrasonically cleaned in ethanol and acetone to remove the solid particles and grease. High purity (99.9999%) argon and nitrogen were used as working gases. The chamber was depressurized to below 7 mPa. During deposition, the substrate temperature was 523.15 K and the working pressure was in 0.5–0.8 Pa. To improve the adhesion between substrate and coating, a thin titanium layer was deposited at 7.7 W·cm^{-2} for 10 minutes followed by transition layers with different atomic ratios of Ti and Nb. Finally, the target powers of Ti and Nb were regulated to 4.4 W·cm^{-2} and held for 2 h to obtain the TiNb coating. The deposition parameters of the TiNbN coating were similar to

that of TiNb with lower temperature (473.15 K). The gas flow volumetric ratio of reactive gas (nitrogen) and inert gas (argon) was set as 1:5. The thicknesses of the TiNb and the TiNbN coatings were about 660 and 2080 nm, respectively, according to coatings' deposition rates.

2.2. Characterization of Coatings

The structures of the TiNb and TiNbN coatings were determined by XRD (D8 Advance, Bruker, GER), using Cu Kα radiation in glancing angle mode at 1°. The scan speed was 2°·min^{-1} with a step size of 0.02°. The surface morphologies of the coatings were characterized by SEM (Merlin, Zeiss Company, GER) equipped with EDS. To evaluate the chemical composition of the coatings, XPS (EscaLab 250XI, Thermo Fisher Scientific, UK) technique was used. The corrosion resistance of the bipolar plate material was tested by electrochemical methods including potentiodynamic polarization, electrochemical impedance spectroscopy (EIS) and potentiostatic polarization in 0.5 mol·L^{-1} H$_2$SO$_4$ solutions saturated with O$_2$ at room temperature, using an electrochemical workstation (CHI760E, Shanghai Chenhua Instruments Limited, CN). The sample size was 20 by 20 mm for the tests. The testing container was a three-electrode cell. Working electrodes were SS samples, sealed by circular rings with a hole of 1 cm^2 exposure area. To avoid the possible addition of adverse reactive ions from other electrodes, a saturated mercurous sulfate electrode (MSE) and a platinum foil served as reference electrode and counter electrode, respectively. Prior to tests, samples were immersed in electrolyte solutions for 30 min to get stable open circuit potential (OCP). The scan rate of potentiodynamic polarization was set as 2 mV·s^{-1}. EIS was carried out at both OCP and 0.19 V vs MSE, within a 0.01–10^5 Hz frequency range and with a 10 mV potential amplitude. Besides electrochemical evaluation, ICR measurements were performed. Two pieces of Toray conductive carbon papers were sandwiched between SS sample (30 by 30 mm) and two Au coated copper plates like Wang's method [25]. An electrical current of 2A was applied via the copper plates. The ICR value between the coating and carbon paper was calculated from the voltage drop and the current with the resistances between the other contact interfaces measured by the similar method subtracted.

3. Results and Discussion

3.1. Structural Characterization

To avoid the possible effects from rough SS substrates, TiNb and TiNbN surface films for structural characterization were deposited on well-polished silicon wafers. The XRD patterns are shown in Figure 1.
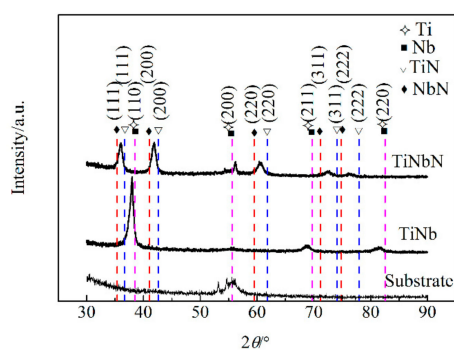

Figure 1. X-ray diffraction (XRD) patterns for TiNb and TiNbN coatings on silicon wafers. The hatched lines indicate peak positions of selected materials. The peaks of cubic Ti and Nb are showed by coinciding lines.

The vertical hatched lines represent peaks recorded in PDF cards No. 38-1155 (cubic NbN), No. 38-1420 (cubic TiN), No. 34-0370 (cubic Nb), and No. 44-1288 (cubic Ti). The diffraction peaks of cubic Nb and Ti are very close and consequently indicated by the same lines. The TiNb film follows the

same patterns suggesting that the alloy has the same cubic structure. It is reasonable to assume a solid solution of Ti and Nb. The angles are shifted to lower values indicating some stress. For the TiNbN coating, the Bragg angles of diffraction peaks are between those of TiN and NbN, which denotes that TiN and NbN are likewise a solid solution [26]. Moreover, diffraction peaks arising from (111), (200), (220), (311), and (222) plane reflections are clearly identified, confirming the face centered cubic (fcc) crystalline structure.

3.2. Surface Morphology

The SEM images of 316L SS, TiNbN/316L SS and TiNb/316L SS before and after potentiostatic polarization corrosion tests are shown in Figure 2.
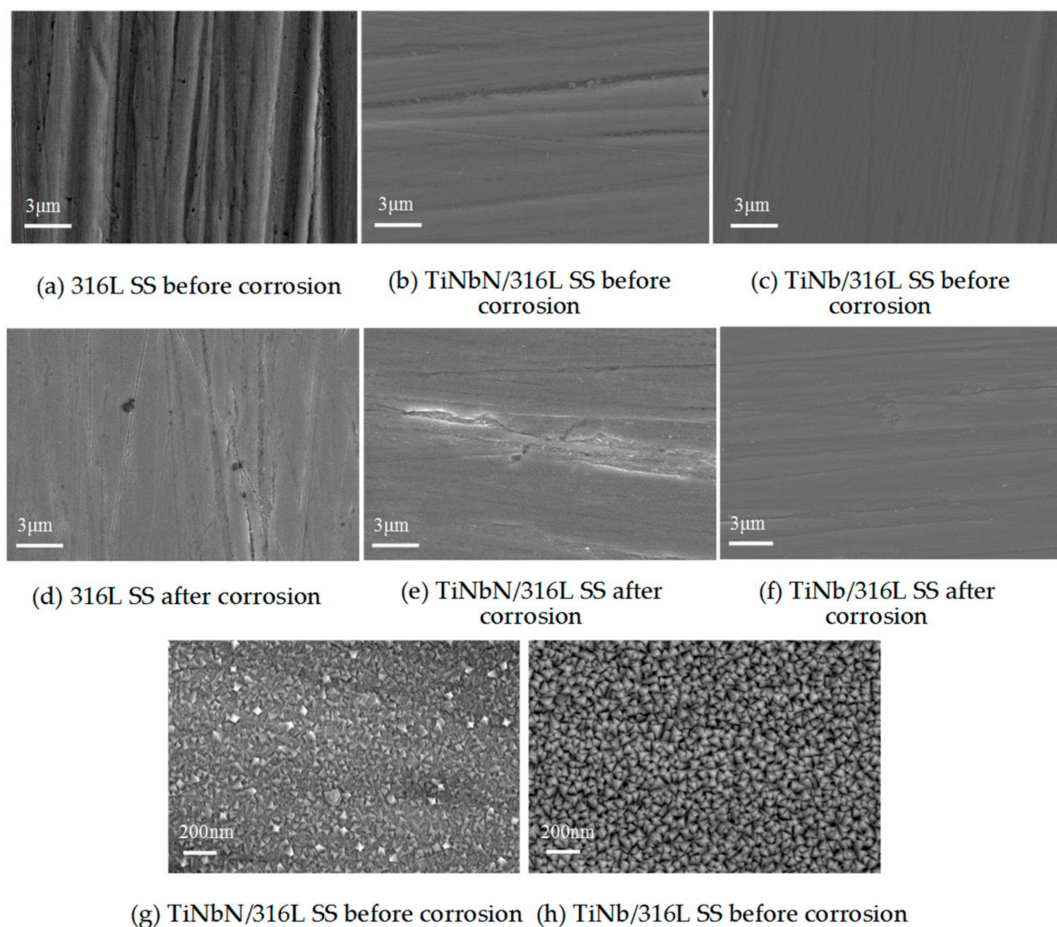

Figure 2. Scanning electron microscopy (SEM) images of the surface of 316L stainless steel (SS), TiNbN/316L SS and TiNb/316L SS.

In Figure 2a, the polished SS surface is uneven due to grinding and polishing, and a number of holes are randomly distributed on it. In Figure 2b, the TiNbN surface is much smoother than that of the SS. However, small holes still exist, and at the bottom of the surface valley, some large particles appear. The micrograph of the TiNb coating shown in Figure 2c is smooth and nearly no obvious holes can be seen. Obviously, the deposition of TiNbN or TiNb has smoothened the SS samples. This may also limit the formation of micro corrosion cells. The morphologies of uncoated and coated 316L SS after potentiostatic polarization tests are shown in Figure 2d–f. After corrosion, 316L SS shows several holes (Figure 2d) which are larger than those observed on 316L SS before corrosion. In Figure 2e, localized corrosion is apparent especially for the valley and defect areas on the TiNbN coating while the surface of TiNb/316L SS in Figure 2f shows few large or deep corrosion pits. This is relevant with the coating defects formed on TiNbN before corrosion. For the hole defect, the electrolyte solution

diffusion at the bottom of it is slow. The concentrations of O_2 and ions inside the hole differ from that in solution, resulting in the different electrochemical activities of grains. Due to the lack of O_2 and the dense passive film, the inner region of the hole becomes the anode of a corrosion battery with a smaller area and a higher corrosion current density, compared with other surface zones. Thus the localized corrosion is induced and more defects are formed. Images in Figure 2g,h under higher magnification indicate that the grain size of sputtering deposited TiNbN varies greatly but with a smaller average value compared with TiNb which might be attributed to the incorporation of N. For the TiNbN coating, the distinction in grain size could result in an inhomogeneous distribution of grain boundaries and finally contributing to the non-uniformity of passive layer [27]. Additionally, the SEM results show the particle agglomeration phenomenon of TiNbN is more serious than of TiNb. And the agglomeration may cause the differences in coating's surface structure and composition by which the localized corrosion of TiNbN can be induced.

In order to characterize the coating composition, EDS was applied and results are shown in Figure 3. Since the coating is thin, the detected images may include intensity peaks from some elements in the substrate, the substrate oxidation layer and adsorbed substances on sample surface. In the film of TiNbN/SS, the atomic ratio of Ti, Nb and N is about 7:22:10 (with the usual reservations regarding quantifications of light elements). For the coating of TiNb/SS, the atomic ratio of Ti and Nb is about 1:4. The EDS results illustrate under the same sputtering power mentioned above, the deposition speed of Nb is faster than that of Ti. Possible reason for this phenomenon is that Nb is a DC power target, and Ti is powered by a RF electric source. For the same material, the sputtering rate of the RF target is lower than that of the DC target at the same set power.
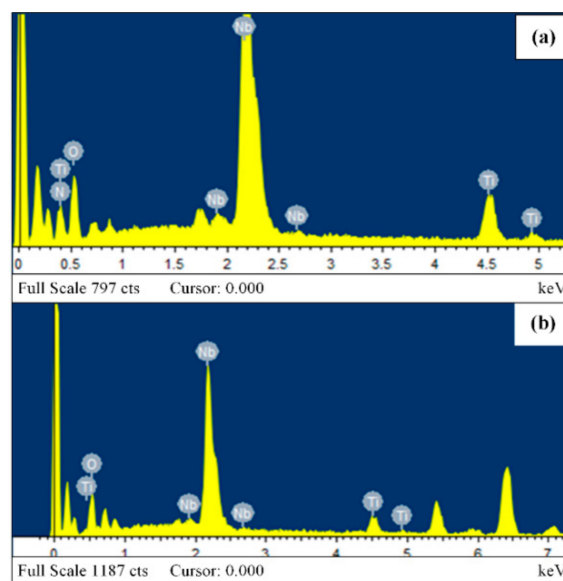

Figure 3. Energy dispersive spectrometry (EDS) results of (**a**) TiNbN/316L SS and (**b**) TiNb/316L SS.
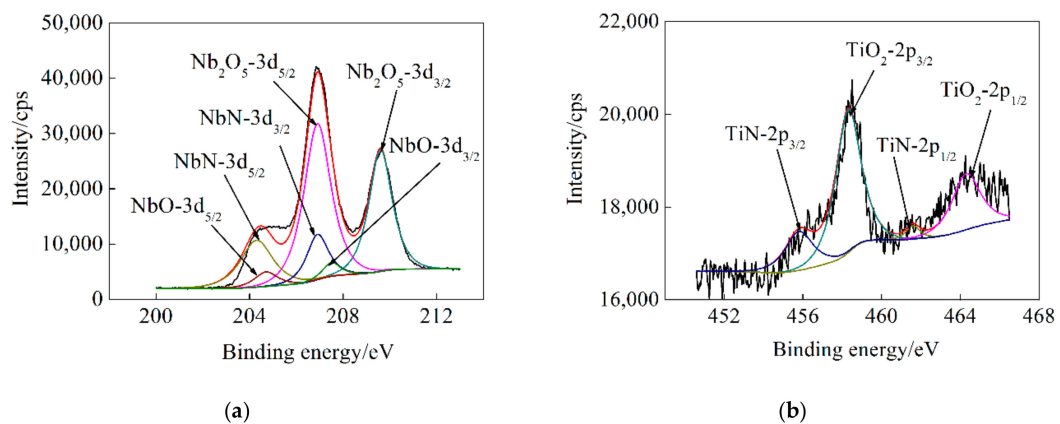
3.3. X-ray Photoelectron Spectroscopy Analysis

The chemical states of Ti and Nb in the surface layers of the TiNb and TiNbN films were examined by XPS. The original Nb 3d and Ti 2p spectra are shown in Figures 4 and 5. After fitting all the spectra with backgrounds subtracted, Nb 3d and Ti 2p peaks were analyzed according to the NIST XPS Database [28], relative literatures and possible reactions in testing environment. In Figure 4a, it's deduced that the highest doublet peaks are related to $3d_{5/2}$ and $3d_{3/2}$ of Nb in Nb_2O_5 and the lower peaks represent metal Nb [29–32]. From the Ti 2p fitted spectra in Figure 4b, two peaks are observed corresponding to Ti $2p_{3/2}$ and Ti $2p_{1/2}$ in TiO_2, respectively [33,34]. The testing results reveal that the surface layer of the TiNb coating is primarily composed of Nb_2O_5 and TiO_2, which means the TiNb coating can be oxidized spontaneously in air and form a stable metallic oxide film. Figure 5 shows XPS

spectra of Nb 3d and Ti 2p of the TiNbN coating. The fitted Nb 3d spectra depicted in Figure 5a indicate that the major peaks representing Nb $3d_{5/2}$ and Nb $3d_{3/2}$ can be ascribed to the formation of Nb_2O_5, NbN, and NbO [31,32,35]. The Ti 2p fitted spectra in Figure 5b reveal the existence of TiN [36]. But the two largest peaks stem from Ti $2p_{3/2}$ and Ti $2p_{1/2}$ in TiO_2 [37,38]. From the fitted results, it is obvious that under the sputtering conditions mentioned above, TiN and NbN were synthesized. Due to the exposure of the coating to air, stable oxides of Ti and Nb were also formed in the outer layer of TiNbN coating. Since the main surface composition difference between TiNb and TiNbN coatings lies in TiN and NbN, metallic nitrides could play an important role in exhibiting some different properties for TiNb/316L SS and TiNbN/316L SS.

(a)　　　　　　　　　　　　　　　(b)
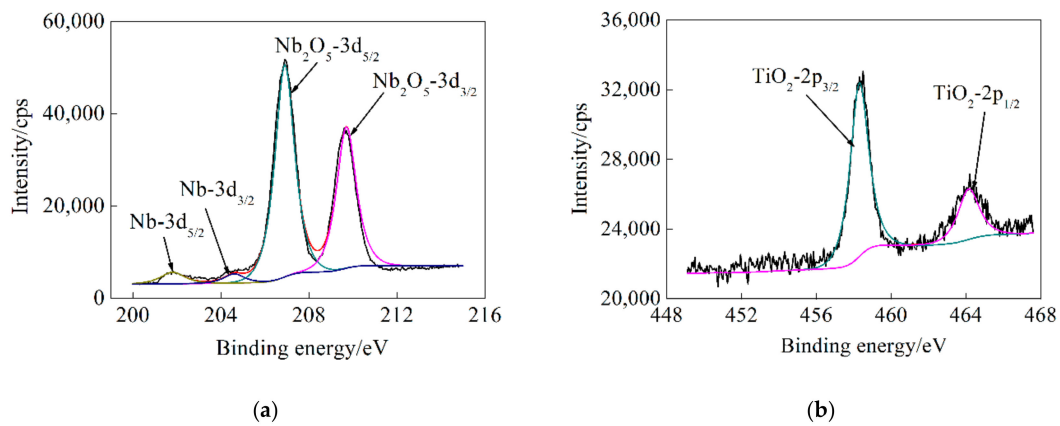
Figure 4. X-ray photoelectron spectroscopy (XPS) spectra of (**a**) Nb 3d and (**b**) Ti 2p (original-black lines, fitted-red lines) measured on TiNb/316L SS.


(a)　　　　　　　　　　　　　　　(b)

Figure 5. X-ray photoelectron spectroscopy (XPS) spectra of (**a**) Nb 3d and (**b**) Ti 2p (original-black lines, fitted-red lines) measured on TiNbN/316L SS.

3.4. Corrosion Behavior

The corrosion behaviors of 316L SS, TiNb/316L SS and TiNbN/316L SS were characterized electrochemically by potentiodynamic polarization, EIS, and potentiostatic polarization. Figure 6 displays potentiodynamic polarization curves of bare and coated 316L SS. From the curves, corrosion potentials (ϕ_{corr}) are obtained. The ϕ_{corr} is related to coating's thermodynamic stability, and the higher ϕ_{corr} value normally means better corrosion resistance from the aspect of thermodynamics [3]. In the tests, the ϕ_{corr} of 316L SS is −0.761 V vs MSE, whereas TiNbN/316L SS has a more positive value of −0.744 V. Compared with the substrate, the TiNb film increases the ϕ_{corr} by 138 mV. When potentials are swept from negative to positive, all three samples show obvious passivation areas. In the passivation area, as the potential value increases, the current density remains nearly constant. At 0.19 V vs MSE, all the samples are passivated and 316L SS exhibits a current

density of 17.3 $\mu A \cdot cm^{-2}$, while it is 2.28 $\mu A \cdot cm^{-2}$ and 44.6 $\mu A \cdot cm^{-2}$ for TiNb/316L SS and TiNbN/316L SS, respectively. The results indicate that the TiNb film has high corrosion resistance at 0.19 V vs MSE. This is owing to the formation of corrosion resistant passive film on TiNb coating obtained from anodic polarization process. Moreover, it is noteworthy that although the TiNbN film is thicker, TiNb alloy establishes better corrosion resistance. This phenomenon is mainly associated with the surface condition and composition of TiNbN film.
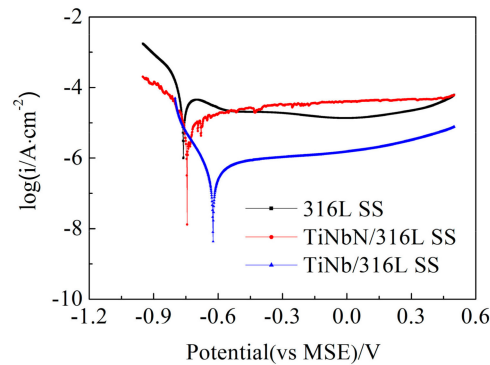

Figure 6. Potentiodynamic polarization curves of 316L SS, TiNb/316L SS, and TiNbN/316L SS.

EIS was performed and Figure 7 shows Nyquist impedance spectra of coated and uncoated 316L SS measured at OCP and 0.19 V vs MSE. In Figure 7a, influenced by surface defects, TiNbN/316L SS shows two time constants at OCP which reflect the impedance information from coating and substrate [12,39]. In the Nyquist impedance spectra of TiNbN/316L SS at 0.19V, TiNb/316L SS, and 316L SS, incomplete semicircular arcs appear. The depressed semicircular shape of SS is attributed to the roughness of sample's surface. To fit the impedance spectrum of TiNbN/316L SS measured at OCP, an equivalent circuit with two constant phase elements (CPE), shown in Figure 8a [40], is adopted. The CPE is represented by Q. Under ideal conditions, a CPE corresponds to a capacitor [41]. R_s is the resistance of electrolyte solution between working electrode and reference electrode. R_f and Q_f are coating's resistance and capacitance, respectively, and R_{ct} is the charge transfer resistance, while Q_1 represents the double layer capacitance [42]. The other spectra in Figure 7a,b are fitted by the equivalent circuit in Figure 8b [43]. Table 1 lists the fitted values of R_{ct}. The higher R_{ct} suggests the enhanced corrosion resistance [44,45].
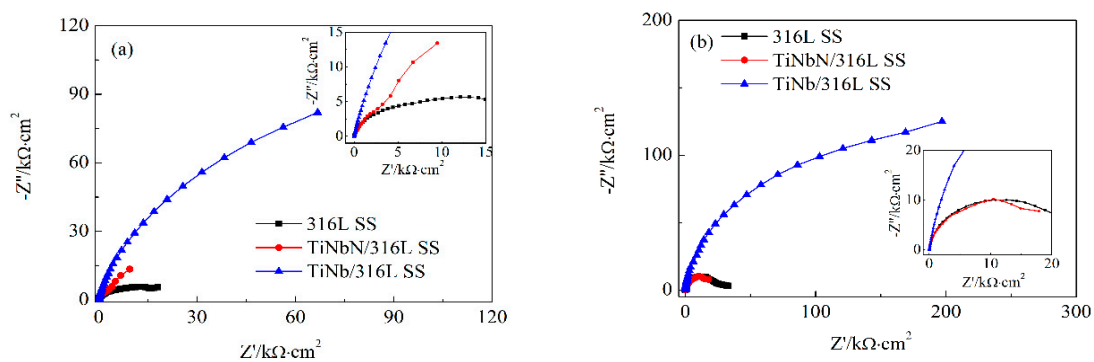
Figure 7. Nyquist impedance spectra of 316L SS, TiNb/316L SS and TiNbN/316L SS @ (**a**) open circuit potential (OCP), (**b**) 0.19 V vs mercurous sulfate electrode (MSE).
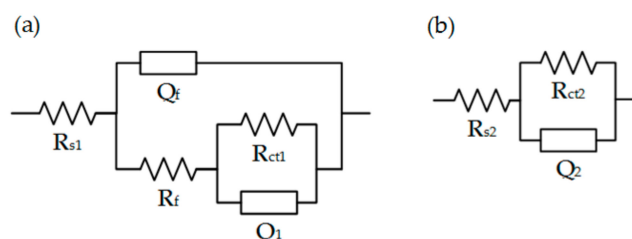
Figure 8. Equivalent circuits used for the Nyquist impedance spectra of (**a**) TiNbN/316L SS @ OCP; (**b**) TiNbN/316L SS @ 0.19 V vs MSE, 316L SS, and TiNb/316L SS.
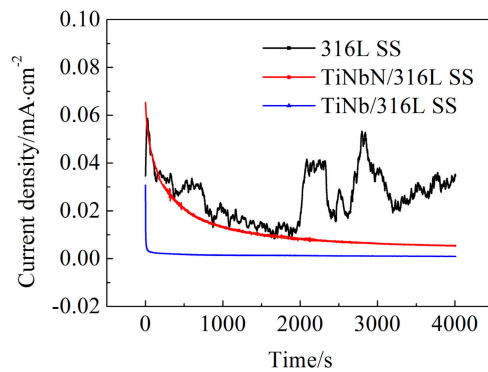
Table 1. R_{ct} values of 316L SS, TiNb/316L SS and TiNbN/316L SS at different potentials.

Materials	316L SS	TiNb/316L SS	TiNbN/316L SS
R_{ct} @ OCP/ $k\Omega \cdot cm^2$	16.2	198	21.13
R_{ct} @ 0.19 V vs MSE/ $k\Omega \cdot cm^2$	26.74	229	23.52

Comparing R_{ct} values of different materials in Table 1, it is observed that the charge transfer impedance of TiNb coated 316L SS is much higher than for the uncoated substrate. Part of reasons for this phenomenon is that the surface layer of TiNb could be oxidized into TiO_2 and Nb_2O_5 spontaneously in air according to XPS measurements, providing a high corrosion resistance. At 0.19 V vs MSE, the high potential and the continuous supply of oxygen could passivate TiNb and lead to the formation of dense passive film which is corrosion resistant and could act as a barrier to inhibit the bulk solution from approaching the sub-layer directly. In comparison with TiNb, the R_{ct} value of the TiNbN film is much smaller, either at OCP or 0.19 V vs MSE. Two major factors may contribute to this phenomenon. From a morphology point of view, the particle clusters and pores observed on the TiNbN coating can cause localized corrosion. The other reason is that the bonds between nitrogen and metallic atoms may impede the formation of more homogeneous and corrosion resistant passive layer. According to the above analysis, from the EIS and potentiodynamic polarization test results draw one can the conclusion that TiNb has good corrosion resistance while TiNbN and bare 316L SS are likely to dissolve in the aggressive cathode environment.

To evaluate the stability of the materials, potentiostatic polarization experiments were conducted at 0.19 V vs MSE. The results are shown in Figure 9. In the beginning, the current density of each coated 316L SS sample declines while that of 316L SS first increases sharply, then decreases gradually. After 2000 s, 316L SS experiences an obvious fluctuation due to the surface states changes affected by electrochemical dissolution, but throughout this period, its average corrosion rate is increasing. As for TiNbN/316L SS, the time needed for total passivation is about 3000 s, and its stabilized current density is approximately 6–7 $\mu A \cdot cm^{-2}$. Although TiNbN/316L SS and 316L SS show comparable current density values and variation trends at the initial stage of tests, the TiNbN coating is much more stable than bare 316L SS, judging from the smoothness of the curves. That is because the coating deposited by magnetron sputtering is uniform and has less defects than the substrate. The current density of TiNb/316L SS decays rapidly first and then stabilizes at 0.9–1 $\mu A \cdot cm^{-2}$. This demonstrates that the TiNb coating can be easily passivated and keep a low corrosion current density for a relatively long period, influenced by the high potential and the oxygen saturated acid solution, which shows the good corrosion resistance and stability of the TiNb coating. From the potentiostatic polarization tests above, it is assumed that TiNb/316L SS has the potential to work as a PEMFC cathode flow plate material for a long time.

Figure 9. Potentiostatic polarization curves of 316L SS, TiNb/316L SS, and TiNbN/316L SS.

The electrochemical testing shows that both TiNb and TiNbN coatings can form steady passive films at 0.19 V vs MSE, and the long-term corrosion current density of TiNb/316L SS is lower than 1 μA· cm^{-2}, illustrating the high corrosion resistance of TiNb coating. Compared with TiNb/316L SS, TiNbN/316L SS is of poorer corrosion resistance.

3.5. Interfacial Contact Resistance

The conductivity of bipolar plates has great impact on the PEMFC's working efficiency [46]. Normally, the bulk resistance of metallic bipolar plates can be ignored since the ICR between the bipolar plate and the carbon paper is much greater. In Figure 10, the ICR of the material with a carbon paper is plotted as a function of the compression force.
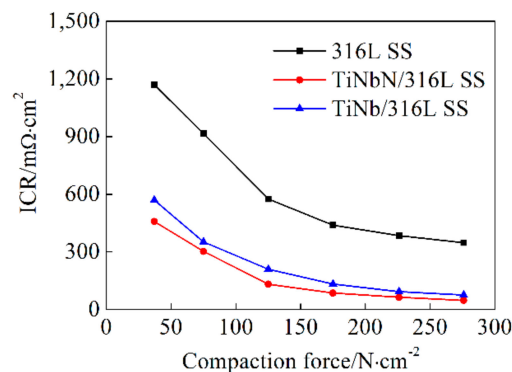
Figure 10. Interfacial contact resistances (ICR) between 316L SS, TiNb/316L SS, TiNbN/316L SS and carbon paper as a function of compaction force.

In the low-force region, as compaction force raises, the contact area between carbon paper and sample increases leading to the decrease of ICR, and when the force is high enough, the ICR is dominated by the surface composition and nature [46,47]. At the same force, the contact resistance of 316L SS, TiNb/316L SS, and TiNbN/316L SS decreases in turn, and their conductivity increases sequentially. I.e., both the TiNb and the TiNbN coatings provide lower ICR than 316L SS's, but the effect of TiNbN is more remarkable. At 276 N·cm^{-2}, TiNbN coating's ICR is approximately 48 mΩ·cm^2, and the ICR value of TiNb/316L SS is nearly 1/5 of that of 316L SS. One of the reasons behind this is that both coatings could reduce the roughness of 316L SS substrate leading to an increased contact area. For the TiNbN coating, the dopant of TiN and NbN in its surface layer improves conductivity. In comparison with TiO$_2$ and Nb$_2$O$_5$, TiN [48] and NbN have higher conductivity. Overall, the TiNbN coating is of relatively high electrical conductivity, and the TiNb film reduces the substrate's ICR. However, considering the moderate corrosion resistance of TiNbN, TiNb/316L SS is more promising for use as bipolar plate. Further studies are relevant assessing a combined film with good conductivity from TiNbN and great corrosion resistance from TiNb.

4. Conclusions

TiNb and TiNbN films with low Ti content were coated on 316L SS by magnetron sputtering with a view to application for bipolar plates in PEMFC. The electrochemical testing indicates that TiNb coating has the best corrosion resistance in cathode simulation electrolyte solutions. At 0.19 V vs MSE, the stable corrosion current density of TiNb/316L SS is lower than 1 $\mu A \cdot cm^{-2}$. The ICR measurements show that the contact conductivity of TiNb/316L SS is higher than that of substrate. Compared with 316L SS and the TiNb coating, TiNbN film shows moderate corrosion resistance but the lowest ICR. According to XRD analysis, the main component of TiNbN is a solid solution of cubic NbN and TiN. The morphologies of TiNb and TiNbN characterized by SEM reveal that both coatings provide smooth surfaces. It can be concluded that the TiNb/316L SS is a kind of promising bipolar plate material with high corrosion resistance. Nevertheless, the conductivity of TiNb/316L SS still needs to be improved. In the future, multilayer coatings consisting of TiNb and TiNbN with optimized atomic ratios will be studied with aim to improve material's corrosion resistance and conductivity further.

References

1. Wang, Y.; Chen, K.S.; Mishler, J.; Cho, S.C.; Adroher, X.C. A review of polymer electrolyte membrane fuel cells: Technology, applications, and needs on fundamental research. *Appl. Energy* **2011**, *88*, 981–1007. [CrossRef]

2. Antunes, R.A.; Oliveira, M.C.L.; Ett, G.; Ett, V. Corrosion of metal bipolar plates for PEM fuel cells: A review. *Int. J. Hydrog. Energy* **2010**, *35*, 3632–3647. [CrossRef]

3. Wang, L.; Tao, Y.; Zhang, Z.; Wang, Y.; Feng, Q.; Wang, H.; Li, H. Molybdenum carbide coated 316L stainless steel for bipolar plates of proton exchange membrane fuel cells. *Int. J. Hydrog. Energy* **2019**, *44*, 4940–4950. [CrossRef]

4. Kim, M.; Lim, J.W.; Lee, D.G. Electrical contact resistance between anode and cathode bipolar plates with respect to surface conditions. *Compos. Struct.* **2018**, *189*, 79–86. [CrossRef]

5. Adloo, A.; Sadeghi, M.; Masoomi, M.; Pazhooh, H.N. High performance polymeric bipolar plate based on polypropylene/graphite/graphene/nano-carbon black composites for PEM fuel cells. *Renew. Energy* **2016**, *99*, 867–874. [CrossRef]

6. Dhakate, S.R.; Sharma, S.; Chauhan, N.; Seth, R.K.; Mathur, R.B. CNTs nanostructuring effect on the properties of graphite composite bipolar plate. *Int. J. Hydrog. Energy* **2010**, *35*, 4195–4200. [CrossRef]

7. Li, W.; Jing, S.; Wang, S.; Wang, C.; Xie, X. Experimental investigation of expanded graphite/phenolic resin composite bipolar plate. *Int. J. Hydrog. Energy* **2016**, *41*, 16240–16246. [CrossRef]

8. Taherian, R. A review of composite and metallic bipolar plates in proton exchange membrane fuel cell: Materials, fabrication, and material selection. *J. Power Sources* **2014**, *265*, 370–390. [CrossRef]

9. Yu, H.; Yang, L.; Zhu, L.; Jian, X.; Wang, Z.; Jiang, L. Anticorrosion properties of Ta-coated 316L stainless steel as bipolar plate material in proton exchange membrane fuel cells. *J. Power Sources* **2009**, *191*, 495–500. [CrossRef]

10. Mawdsley, J.R.; Carter, J.D.; Wang, X.; Niyogi, S.; Fan, C.Q.; Koc, R.; Osterhout, G. Composite-coated aluminum bipolar plates for PEM fuel cells. *J. Power Sources* **2013**, *231*, 106–112. [CrossRef]

11. Bi, F.; Peng, L.; Yi, P.; Lai, X. Multilayered Zr–C/a-C film on stainless steel 316L as bipolar plates for proton exchange membrane fuel cells. *J. Power Sources* **2016**, *314*, 58–65. [CrossRef]

12. Mani, S.P.; Rajendran, N. Corrosion and interfacial contact resistance behavior of electrochemically nitrided 316L SS bipolar plates for proton exchange membrane fuel cells. *Energy* **2017**, *133*, 1050–1062. [CrossRef]

13. Asri, N.F.; Husaini, T.; Sulong, A.B.; Majlan, E.H.; Daud, W.R.W. Coating of stainless steel and titanium bipolar plates for anticorrosion in PEMFC: A review. *Int. J. Hydrog. Energy* **2017**, *42*, 9135–9148. [CrossRef]

14. Wind, J.; Spah, R.; Kaiser, W.; Bohm, G. Metallic bipolar plates for PEM fuel cells. *J. Power Sources* **2002**, *105*, 256–260. [CrossRef]

15. Tsai, S.Y.; Bai, C.Y.; Lin, C.H.; Shi, G.N.; Hou, K.H.; Liu, Y.M.; Ger, M.D. The characteristics and performance of electroless nickel and immersion Au plated aluminum alloy bipolar plates in polymer electrolyte membrane fuel cells. *J. Power Sources* **2012**, *214*, 51–58. [CrossRef]

16. Wang, C.; Wang, S.; Peng, L.; Zhang, J.; Shao, Z.; Huang, J.; Sun, C.; Ouyang, M.; He, X. Recent progress on the key materials and components for proton exchange membrane fuel cells in vehicle applications. *Energies* **2016**, *9*, 603. [CrossRef]

17. Wang, L.; Sun, J.; Li, P.; Jing, B.; Li, S.; Wen, Z.; Ji, S. Niobized AISI 304 stainless steel bipolar plate for proton exchange membrane fuel cell. *J. Power Sources* **2012**, *208*, 397–403. [CrossRef]

18. Zhang, D.; Duan, L.; Guo, L.; Tuan, W.H. Corrosion behavior of TiN-coated stainless steel as bipolar plate for proton exchange membrane fuel cell. *Int. J. Hydrog. Energy* **2010**, *35*, 3721–3726. [CrossRef]

19. Cha, B.C.; You, Y.Z.; Hong, S.T.; Kim, J.H.; Kim, D.W.; Lee, B.S.; Kim, S.K. Nitride films as protective layers for metallic bipolar plates of polymer electrolyte membrane fuel cell stacks. *Int. J. Hydrog. Energy* **2011**, *36*, 4565–4572. [CrossRef]

20. Serro, A.P.; Completo, C.; Colaço, R.; dos Santos, F.; da Silva, C.L.; Cabral, J.M.S.; Araújo, H.; Pires, E.; Saramago, B. A comparative study of titanium nitrides, TiN, TiNbN and TiCN, as coatings for biomedical applications. *Surf. Coat. Technol.* **2009**, *203*, 3701–3707. [CrossRef]

21. Gispert, M.P.; Serro, A.P.; Colaço, R.; Pires, E.; Saramago, B. Wear of ceramic coated metal-on-metal bearings used for hip replacement. *Wear* **2007**, *263*, 1060–1065. [CrossRef]

22. Saud, S.N.; Hosseinian, R.; Bakhsheshi-Rad, H.R.; Yaghoubidoust, F.; Iqbal, N.; Hamzah, E.; Ooi, C.H.R. Corrosion and bioactivity performance of graphene oxide coating on Ti-Nb shape memory alloys in simulated body fluid. *Mater. Sci. Eng. C Mater. Biol. Appl.* **2016**, *68*, 687–694. [CrossRef] [PubMed]

23. Aukland, N.; Boudina, A.; Eddy, D.S.; Mantese, J.V.; Thompson, M.P.; Wang, S.S. Alloys that form conductive and passivating oxides for proton exchange membrane fuel cell bipolar plates. *J. Mater. Res.* **2004**, *19*, 1723–1729. [CrossRef]

24. Yi, P.; Zhu, L.; Dong, C.; Xiao, K. Corrosion and interfacial contact resistance of 316L stainless steel coated with magnetron sputtered ZrN and TiN in the simulated cathodic environment of a proton-exchange membrane fuel cell. *Surf. Coat. Technol.* **2019**, *363*, 198–202. [CrossRef]

25. Wang, H.; Sweikart, M.A.; Turner, J.A. Stainless steel as bipolar plate material for polymer electrolyte membrane fuel cells. *J. Power Sources* **2003**, *115*, 243–251. [CrossRef]

26. Xu, J.; Huang, H.J.; Li, Z.Y.; Xu, S.; Tao, H.; Munroe, P.; Xie, Z.H. Corrosion behavior of a ZrCN coated Ti alloy with potential application as a bipolar plate for proton exchange membrane fuel cell. *J. Alloys Compd.* **2016**, *663*, 718–730. [CrossRef]

27. Gollapudi, S. Grain size distribution effects on the corrosion behaviour of materials. *Corros. Sci.* **2012**, *62*, 90–94. [CrossRef]

28. National Institute of Standards and Technology. NIST X-ray Photoelectron Spectroscopy Database, NIST Standard Reference Database Number 20. Available online: https://srdata.nist.gov/xps/ (accessed on 15 April 2019).

29. Bahl, M.K. ESCA studies of some niobium compounds. *J. Phys. Chem. Solids* **1975**, *36*, 485–491. [CrossRef]

30. Nyholm, R.; Martensson, N. Core level binding energies for the elements Zr-Te (Z = 40–52). *J. Phys. C Solid St. Phys.* **1980**, *13*, L279–L284. [CrossRef]

31. Nefedov, V.I.; Salyn, Y.V.; Chertkov, A.A.; Padurets, L.N. X-ray electron study of electron-density distribution in hydrides of transition-elements. *Zh. Neorg. Khim.* **1974**, *19*, 1443–1445.

32. Latta, E.E.; Ronay, M. Catalytic-oxidation of niobium. *Phys. Rev. Lett.* **1984**, *53*, 948–951. [CrossRef]

33. Blasco, T.; Camblor, M.A.; Corma, A.; Perez-Pariente, J. The state of Ti in titanoaluminosilicates isomorphous with zeolite β. *J. Am. Chem. Soc.* **1993**, *115*, 11806–11813. [CrossRef]

34. Sanjinés, R.; Tang, H.; Berger, H.; Gozzo, F.; Margaritondo, G.; Lévy, F. Electronic structure of anatase TiO_2 oxide. *J. Appl. Phys.* **1994**, *75*, 2945–2951. [CrossRef]

35. Zhang, L.; You, L.; Ying, L.; Peng, W.; Wang, Z. Characterization of surface oxidation layers on ultrathin NbTiN films. *Phys. C Supercond. Appl.* **2018**, *545*, 1–4. [CrossRef]

36. Shulga, Y.M.; Troitskii, V.N.; Aivazov, M.I.; Borodko, Y.G. X-ray photoelectron-spectra of scandium, titanium, vanadium and chromium mononitrides. *Zh. Neorg. Khim.* **1976**, *21*, 2621–2624.

37. Netterfield, R.P.; Martin, P.J.; Pacey, C.G.; Sainty, W.G.; McKenzie, D.R.; Auchterlonie, G. Ion-assisted deposition of mixed TiO_2-SiO_2 films. *J. Appl. Phys.* **1989**, *66*, 1805–1809. [CrossRef]

38. Fierro, J.L.G.; Arrua, L.A.; Nieto, J.M.L.; Kremenic, G. Surface properties of co-precipitated V-Ti-O catalysts and their relation to the selective oxidation of isobutene. *Appl. Catal.* **1988**, *37*, 323–338. [CrossRef]

39. Jeon, W.S.; Kim, J.G.; Kim, Y.J.; Han, J.G. Electrochemical properties of TiN coatings on 316L stainless steel separator for polymer electrolyte membrane fuel cell. *Thin Solid Films* **2008**, *516*, 3669–3672. [CrossRef]

40. Cao, M.; Liu, L.; Yu, Z.; Fan, L.; Li, Y.; Wang, F. Electrochemical corrosion behavior of 2A02 Al alloy under an accelerated simulation marine atmospheric environment. *J. Mater. Sci. Technol.* **2019**, *35*, 651–659. [CrossRef]

41. Kartsonakis, I.A.; Stanciu, S.G.; Matei, A.A.; Karaxi, E.K.; Hristu, R.; Karantonis, A.; Charitidis, C.A. Evaluation of the protective ability of typical corrosion inhibitors for magnesium alloys towards the Mg ZK30 variant. *Corros. Sci.* **2015**, *100*, 194–208. [CrossRef]

42. Nam, N.D.; Jo, D.S.; Kim, J.G.; Yoon, D.H. Corrosion protection of CrN/TiN multi-coating for bipolar plate of polymer electrolyte membrane fuel cell. *Thin Solid Films* **2011**, *519*, 6787–6791. [CrossRef]

43. Li, M.; Luo, S.; Zeng, C.; Shen, J.; Lin, H.; Cao, C. Corrosion behavior of TiN coated type 316 stainless steel in simulated PEMFC environments. *Corros. Sci.* **2004**, *46*, 1369–1380. [CrossRef]

44. Kartsonakis, I.A.; Stanciu, S.G.; Matei, A.A.; Hristu, R.; Karantonis, A.; Charitidis, C.A. A comparative study of corrosion inhibitors on hot-dip galvanized steel. *Corros. Sci.* **2016**, *112*, 289–307. [CrossRef]

45. Shen, S.; Zuo, Y.; Zhao, X. The effects of 8-hydroxyquinoline on corrosion performance of a Mg-rich coating on AZ91D magnesium alloy. *Corros. Sci.* **2013**, *76*, 275–283. [CrossRef]

46. Xu, J.; Li, Z.Y.; Xu, S.; Munroe, P.; Xie, Z.H. A nanocrystalline zirconium carbide coating as a functional corrosion-resistant barrier for polymer electrolyte membrane fuel cell application. *J. Power Sources* **2015**, *297*, 359–369. [CrossRef]

47. Feng, K.; Li, Z.; Sun, H.; Yu, L.; Cai, X.; Wu, Y.; Chu, P.K. C/CrN multilayer coating for polymer electrolyte membrane fuel cell metallic bipolar plates. *J. Power Sources* **2013**, *222*, 351–358. [CrossRef]

48. Lee, E.K.; Kim, J.K.; Kim, T.J.; Song, H.; Kim, J.H.; Park, S.A.; Jeong, T.G.; Yun, S.W.; Lee, J.; Goo, J.; et al. Enhanced corrosion resistance and fuel cell performance of Al1050 bipolar plate coated with TiN/Ti double layer. *Energy Convers. Manag.* **2013**, *75*, 727–733. [CrossRef]